

Niclosamide reverses SARS-CoV-2 control of lipophagy

Timothy J. Garrett^{1,2*}, Heather Coatsworth^{3‡}, Iqbal Mahmud^{1,2‡}, Timothy Hamerly^{3‡}, Caroline J. Stephenson^{3,4}, Hoda S. Yazd⁵, Jasmine Ayers³, Megan R. Miller³, John A. Lednicky^{3,4}, Rhoel R. Dinglasan^{3*}

¹Department of Pathology, Immunology, and Laboratory Medicine, College of Medicine, University of Florida, Gainesville, FL, 32610 USA

²Southeast Center for Integrated Metabolomics, Clinical and Translational Science Institute, University of Florida, Gainesville, FL, 32610 USA

³Emerging Pathogens Institute, Department of Infectious Diseases and Immunology, College of Veterinary Medicine, University of Florida, Gainesville, FL, 32611 USA

⁴Department of Environmental and Global Health, College of Public Health and Health Professions, University of Florida, Gainesville, FL, 32610 USA

⁵Department of Chemistry, University of Florida, Gainesville, FL 32603 USA

*Co-corresponding authors: tgarrett@ufl.edu and rdinglasan@epi.ufl.edu

‡Authors contributed equally.

SUMMARY

The global effort to combat COVID-19 rapidly produced a shortlist of approved drugs with antiviral activities for clinical repurposing. However, the jump to clinical testing was lethal in some cases as a full understanding of the mechanism of antiviral activity as opposed to pleiotropic activity/toxicity for these drugs was lacking. Through parallel lipidomic and transcriptomic analyses we observed massive reorganization of lipid profiles of infected Vero E6 cells, especially plasmalogens that correlated with increased levels of virus replication. Niclosamide (NIC), a poorly soluble anti-helminth drug identified for repurposed treatment of COVID-19, reduced the

total lipid profile that would otherwise amplify during virus infection. NIC treatment reduced the abundance of plasmalogens, diacylglycerides, and ceramides, which are required for virus production. Future screens of approved drugs may identify more druggable compounds than NIC that can safely but effectively counter SARS-CoV-2 subversion of lipid metabolism thereby reducing virus replication. However, these data support the consideration of niclosamide as a potential COVID-19 therapeutic given its modulation of lipophagy leading to the reduction of virus egress and the subsequent regulation of key lipid mediators of pathological inflammation.

Keywords: lipidomics, autophagy, lipophagy, SARS-CoV-2, coronavirus, COVID-19, mass spectrometry, RNA sequencing, niclosamide, antivirals, metabolism, chemical biology

INTRODUCTION

The current pandemic spread of SARS-CoV-2 has resulted in >600,000 deaths in the United States alone and >176M cases and >3.8M deaths worldwide (Dong et al., 2020). In 2020, there was a rapid global effort to study severe acute respiratory syndrome coronavirus 2 (SARS-CoV-2) infection kinetics *in vitro* to identify pathways that are involved in entry, replication, and egress of the virus as new targets that can be treated with existing drugs (Gautret et al., 2020; Jeon et al., 2020; Liu et al., 2020; Vincent et al., 2005; Wang et al., 2020; Zhou et al., 2020). However, this worldwide effort was fraught with inconsistencies ranging from the mammalian host cell used for infection studies, to overall study design, which made it difficult to identify common host cell pathways critical to virus biology that can be targeted with available compounds.

Chloroquine (CQ) and, hydroxychloroquine (HCQ), which are indicated for treating malaria, have been shown to also have antiviral activity against SARS-CoV-2 (D'Alessandro et al.,

2020; Dyllal et al., 2014; Liu et al., 2020; Mauthe et al., 2018; Vincent et al., 2005; Wang et al., 2020). However, the direct and rapid translation of this finding to clinical studies during the pandemic was either equivocal at best, or disastrous (Axfors et al., 2021). Although no studies to date have specifically and comprehensively explored the underlying antiviral mechanism of action (MOA) for these two drugs, they nonetheless moved quickly to COVID-19 clinical studies. CQ and HCQ are 4-aminoquinolines (4-AQ), and another human-safe 4-AQ drug, Amodiaquine (AQ), has also been shown to have antiviral activity against SARS-CoV-1 and Middle East respiratory syndrome coronavirus (MERS-CoV) (Dyllal et al., 2014; Vincent et al., 2005), as well as Ebola (D'Alessandro et al., 2020), suggesting that there are common MOAs underpinning broad 4-AQ antiviral activity. Initially, these 4-AQ compounds were considered as candidate partner drugs that can be used along with remdesivir (Wang et al., 2020), the leading broad-spectrum RNA synthesis inhibitor that has shown some clinical benefit (Goldman et al., 2021). The exact nature of the cellular pathways and processes that are targeted by these 4-AQs resulting in reductions in virus propagation remain unknown, but direct protein interaction studies with CQ suggest broad pleiotropic effects on the cell (Gordon et al., 2020). The pleiotropic effects of drugs such as CQ should have given pause, preventing its quick translation to the clinic wherein higher doses of this drug exacerbate the pleiotropic side effects that can result in direct harm to the subject in clinical trials (Borba et al., 2020).

Another anti-parasitic drug, niclosamide (NIC), which suppresses MERS-CoV propagation by inhibiting autophagosome-lysosome fusion through the Beclin1 (Bec1, autophagy regulator/antiapoptotic protein)-SKP2 (S-phase kinase-associated protein 2) pathway (Gassen et al., 2019) has also been proposed to be a potent candidate drug for repurposing in the treatment of SARS-CoV-2 (Xu et al., 2020). NIC is a salicylanilide, oral anti-helminthic drug used in

human and veterinary medicine. Akin to the 4-AQs, it appears to have functional effects beyond the Bec1-SKP2 axis in a cell, resulting in broad anti-infective properties, and as a result, also suffers from poor translational potential to the clinic for COVID-19. Considering the failure of CQ and HCQ to progress towards clinical utility, the candidacy of NIC, which is at an earlier stage of consideration for COVID-19 treatment, compelled us to examine more closely its global effects on host cells to determine if we can uncouple the reported antiviral MOA via the Bec1-SKP2 pathway as well as other putative antiviral mechanisms from intrinsic cytotoxicity. We hypothesize that NIC exerts pleiotropic functional activities on a host cell that result in the perturbation of two intimately associated cellular pathways: autophagy and lipid metabolism. These two processes are dysregulated at critical SARS-CoV-2 life cycle checkpoints during virus infection (Stukalov et al., 2021), and treatment with NIC is hypothesized to reverse this dysregulation. Recently, a multi-omics analysis of clinical samples from COVID-19 patients also described a marked change in lipidomics profiles that correlated with disease severity (Overmyer et al., 2021), but this approach could not characterize the mechanism at the cellular level. Herein, we identified and characterized autophagic or lipophagic pathways (and wider linked cellular networks) that are targeted by NIC in the presence and absence of a SARS-CoV-2 infection. We used the lipid signatures induced by this anti-parasitic compound to detect pathways that are predicted to either lead to direct antiviral effects or to cellular dysregulation and cell death. We discuss the utility of this approach in informing the selection of repurposed drugs that may have more clinical benefit, better bioavailability, and lesser cytotoxicity in the context of COVID-19 and other infectious diseases.

77

78 RESULTS

SARS-CoV-2 infection alters the host cell lipidome

The mechanism by which SARS-CoV-2 enters host cells and systematically alters the cellular environment is currently one of the most compelling areas of study to support the development of antiviral interventions (V'kovski et al., 2020). Evidence suggests that SARS-CoV-2 subverts pre-existing cellular lipids and lipid signaling mechanisms for entry, intracellular trafficking and egress (Abu-Farha et al., 2020). This is consistent with what is known about viruses in general (Mazzon and Mercer, 2014). To investigate the role of lipids in SARS-CoV-2 during the infection cycle in host cells, we profiled the global lipidome from Vero E6 cells at 16h and 48h post-infection with SARS-CoV-2 (**Figure S1A**). The correlation matrix across the groups studied showed a distinct clustering in SARS-CoV-2 infected cells as well as clear clustering with virus and NIC treatment (**Figure S1B**). In addition, a principal component analysis (PCA) revealed clear clustering based on lipid profiles between early (16h) and late (48h) timepoints post viral infection (**Figure S1C**). PCAs also showed clustering with NIC treatment of virus infected cells at early (16h) and late timepoints (48h) (**Figures S1D and E, respectively**). Measurement of supernatant SARS-CoV-2 genome copy with RT-qPCR revealed a significantly higher quantity of released progeny genomes at 48h than 16h, indicating that more viral egress is occurring at the 48h timepoint, which is consistent with literature (**Figure S2**). We did not perform any measurements of infectious progeny virions (i.e., plaque assay), so the antiviral effect of NIC in this experiment cannot be conclusively determined.

As SARS-CoV-2 infection caused perturbations in the global lipid profiles (**Figure 2A**), we next sought to characterize the modulations of different lipid classes between early (16h) vs late (48h) timepoints post viral infection. In total, we identified 720 lipids from 34 classes (**Table S2, S3**) in SARS-CoV-2 infected host cells covering all major lipid classes (**Figure 2A**).

102 Phosphatidylcholine (PC), phosphatidylethanolamine (PE), plasmalogens (ether linked lipids)
103 and triacylglycerol (TG) represented the most frequent lipid classes identified, which is ex-
104 pected given their abundance in cell membranes and lipid droplets (**Figure 2A, Figure 3**).

105 Hierarchical clustering analysis of the differentially regulated lipids ($FC > 1.5$, adjusted p-
106 value < 0.05) revealed specific lipid classes were associated with early or late events during
107 productive virus infection (**Figure 2A, Table S2**). We found that ether lipids including
108 plasmalogen-TG, plasmalogen-TG, plasmalogen-LPC, plasmalogen-PC, plasmalogen-PC, and plasmalogen-
109 PE, as well as diacylglycerides were elevated at 48h post viral infection (**Figure 2B, Table**
110 **S3**). We measured the relative abundance of the total ether linked lipids and observed a highly
111 significant elevation ($P\text{-value} = 2.94E-38$) of total ether linked lipids at 48h post viral infection
112 (**Figure 2C, Figure S3**), suggesting a potential role of ether linked lipids in SARS-CoV-2 path-
113 ogenesis. A comparative extracted ion chromatogram of plasmalogen-PC (O-18:0/16:0)+H, as an
114 example of a specific ether lipid is shown (**Figure 2D**) to convey the clear difference in profiles
115 between the two time points tested. On the other hand, TGs, cholesterol esters (CE), and
116 hexosylceramides (HexCer) were elevated at early stages of infection (16h) (**Figure 2A and B,**
117 **Figure 3, Figure S3, Table S3**). The repertoire of lipid classes that partitioned to early steps in
118 virus infection (16h) and later stages of increased virus replication and egress (48h) are shown
119 in **Figure 3**.

120 Lipids that contained longer chain fatty acids with higher degrees of unsaturation includ-
121 ing TGs (4-9 double bonds (db)), PC (4-5 db), CL (5-6 db), PE (1-6 db), and PS (1-4 db) were
122 elevated in early (16h) viral infection (**Figure 3, Table S3**), a trend consistent with what was
123 described in SARS-CoV-2 infected golden Syrian hamsters (Rizvi et al., 2021). In contrast,
124 saturated fatty acids (SFA), monounsaturated fatty acids (MUFA) and long chain fatty acids

(LCFA) were found to be significantly downregulated in early (16h) viral infection but elevated at 48h post viral infection (**Table S3**), consistent with previous reports (Koyuncu et al., 2013; Nguyen et al., 2018). We identified changes in lipids that may be related to a cellular response to compensate for virus energy utilization, viral particle formation from lipid droplets, vesicle transport and autophagosome formation, noting a significant increase in plasmalogens (ether lipids), sphingolipids (SM and CerNS), glycerophospholipids (PI, PS and PG), lysophospholipids (LPE) and glycerolipids (DG) and a significant decrease in TG and CE lipids at 48h (**Figure 2A-B, Figure 3**).

We observed a differential regulation of lipids during increased levels of viral replication. Of note, we observed significant increases in PG, PS and PI, but not a significant change in PC or PE phospholipids. This differential regulation of phospholipids could suggest formation of membranes for the viral envelope as most mammalian cells are high in PC and PE phospholipids (Deng and Angelova, 2021). The significant decrease in TGs and CEs is likely related to virus utilization of lipid droplets to make viral particles needed for replication. Lipid droplets are used by cells to store neutral lipids that are utilized for energy needs, but viruses require these lipids for replication and thus hijack the lipid droplets to enable their own growth. The increase in plasmalogens is also associated with viral replication and increased levels have been detected in the serum of patients with ZIKV and other viruses (Cloherty et al., 2020; Mazzon and Mercer, 2014).

144

Niclosamide treatment distinctly impacted ether lipids and this effect correlated with increased viral replication and virus egress

To understand these lipid modulations in the context of therapeutic potential, we used niclosamide (NIC), an anti-parasitic drug, which was found to suppress MERS-CoV propagation by enhancing autophagic flux through the Beclin1 (autophagy regulator/antiapoptotic protein)-SKP2 (S-phase kinase-associated protein 2) pathway (Gassen et al., 2019). NIC has also been proposed to be a potent candidate drug for repurposing in the treatment of SARS and COVID-19 (Gassen et al., 2021; Pindiprolu and Pindiprolu, 2020; Wu et al., 2004). The influence of SARS-CoV-2 infection on Vero E6 cell lipid metabolism, and inhibition of autophagic flux encouraged us to assess if NIC may impart therapeutic potential to SARS-CoV-2 infection.

We first examined the effect of NIC on Vero E6 cells in the absence of infection to establish a baseline for both the 16h and 48h time points (**Figure 4, Figure S4, Table S7**). In total, we identified 520 lipids across all samples, with distinct profiles between DMSO control and NIC treated cells. We observed a profound reduction across both time points in the lipid profiles for TG, and this effect was more pronounced at the 48h time point (**Figure 4A**). In the absence of NIC treatment, plasmalogens (plasmanyl-PE, -TG, and -PC as well as plasmenyl-LPC, -PE, -LPE, -PC and -TG) were found to be differentially abundant at 48h as compared to 16h, which is expected given the cell growth during this time frame (**Figure 4A and Table S4**). However, at the 48h time point (24h post treatment) NIC reduced the abundance (>2 log₂ fold-change) of HexCer-NDS, while in parallel, increased the abundance (>2 log₂ fold-change) of plasmenyl- and plasmanyl-TG, PI, plasmanyl-PE and -PC, as well as BMPs (**Figure 4B and Figure S5**).

Having established a baseline effect of NIC on lipid metabolism in Vero E6 cells, we next sought to understand the effect of NIC on lipid metabolism during SARS-CoV-2 infection. We globally profiled lipids from cells infected with SARS-CoV-2 and treated with DMSO as

170 compared to cells infected with SARS-CoV-2 and treated with NIC at 16h (**Figure S1B**) and
 171 48h (**Figure 5A, Figure S1E**) using our UHPLC-HRMS approach. A PCA identified a clear
 172 separation between NIC treated and untreated SARS-CoV-2 infected samples (**Figure S1B, D**
 173 **and E**). We observed that the treatment of Vero E6 cells with NIC for 24h starting 24h after
 174 SARS-CoV-2 infection (48h) robustly impacted the global lipid profile as compared to NIC
 175 treatment beginning simultaneously with SARS-CoV-2 infection (**Figure 5B**), suggesting that
 176 the antiviral activity of NIC is also dependent on host cell state (in this case, infection as op-
 177 posed to cell growth described above), which in turn correlated with higher levels of virus repli-
 178 cation and virion production (**Figure S2**). However, no significant reduction in viral genome
 179 copy was observed in (NIC) treated cells compared to DMSO controls at either timepoint (**Fig-**
 180 **ure S2**). This corroborates previous findings that NIC does not act to inhibit virus entry or ge-
 181 nome replication (Gassen et al., 2021; Pindiprolu and Pindiprolu, 2020). NIC reduced DG as
 182 well as several plasmalogens, both of which would have otherwise been increased by SARS-
 183 CoV-2 infection at the 48h time point (**Figure 5A, Figure 2, Figure 3**). Strikingly, we observed
 184 that NIC treatment downregulated total ether lipids ($P= 2.49E-38$) (**Figure 5C**), suggesting that
 185 NIC may impart anti-viral effect via affecting ether lipid metabolism. As indicated earlier, we
 186 observed an increase in ether lipids at 48h in cells infected with virus alone, suggesting a key
 187 role of ether lipids in viral replication (**Figure 2C**). Upon treatment with NIC, it appears that this
 188 lipid pathway is disrupted significantly, and thus may be affecting viral replication.

189

190 **Transcriptional profiling captures the broader cellular impact of virus infection and**
 191 **treatment with niclosamide**

We assessed if virus-induced changes in lipidomic profiles corresponded to canonical transcriptional regulation of genes that are known to be involved in lipid metabolism, autophagy, phosphorylation, and vesicle transport. Furthermore, we explored if treatment with NIC alters this profile, and whether time of NIC addition alters the course of infection. To do this, we used RNASeq to capture the global cellular gene expression of i) Vero E6 cells over time (effect of time), ii) Vero E6 cells during cellular SARS-CoV-2 infection (effect of virus) and iii) following treatment with NIC (effect of drug).

We did not observe any significantly differentially expressed (DE) genes over time in our Vero E6 culture alone (0h vs 16h, 0h vs 48h, 16h vs 48h) (**Table S6**), suggesting while the cellular background of Vero E6 cells during these different time periods may be dynamic, the age of the cell culture did not confound other comparisons made in this study. Similarly, we did not observe any differences between cells treated with SARS-CoV-2 and NIC at 16h versus 48h. We did, however, observe differences with NIC treated cells at 16h versus 48h (860 DE genes, 474 up-regulated and 386 down-regulated at 48h) (**Table S1B, Table S6**), as well as SARS-CoV-2 infected cells at 16h versus 48h (109 DE genes, 48 up-regulated and 61 down-regulated at 48h) (**Table S1B, Table S6**).

SARS-CoV-2 infection resulted in significantly DE genes across all our comparison groups (**Table S1B, Table S5, Figure 6**). Viral infection resulted in 585 DE genes at 16h (474 up-regulated; 111 down-regulated), and 562 DE genes at 48h (433 up-regulated; 129 down-regulated) (**Table S5**). SARS-CoV-2 and NIC conditions resulted in more DE genes than SARS-CoV-2 infection alone; NIC and viral infection resulted in 3,083 DE genes (1,301 up-regulated; 1,782 down-regulated) at 16h, and 1,595 DE genes (706 up-regulated, 889 down-regulated) at 48h (**Table S5**). Overrepresented GO terms associated in both up- and down-

regulated DE datasets contained a large number of lipid phosphate metabolism, lipid transport, autophagy and lysosome-associated terms. Terms related to phosphatidylinositol, phosphatidylethanolamine and phosphatidylglycerol were especially prevalent, mirroring observed changes in the lipidomics data. At 16h, viral infection induced an up-regulation of GABARAPL1, MAP1LC3A, PIK3C3, USP30-ORG3a and TBK1 (also up-regulated at 48h), and a down-regulation of STK11, LARP1, ZC3H12A, TFEB, TICAM1, GOLGA2, PIK3R2, IFI16, ULK1, WDR81, SQSTM1 (also down-regulated at 48h), and HK2. As per viral infection, NIC and virus treated cells (at 48h) also saw an up-regulation of GABARAPL1, MAP1LC3A, USP30-ORG3a, BMF, and TBK1; WDR81 was also down-regulated in the NIC and virus treatment at 48h.

There were significant transcriptomic differences noted at 16h and 48h with NIC treatment (**Figures 6E and F**), and at 48h with NIC treatment and SARS-CoV-2 infection (**Table S1B, Table S7, Figure 6G**). NIC treatment alone induced 2,447 DE genes at 16h (1,301 up-regulated; 1,146 down-regulated), and 2846 genes at 48h (1,707 up-regulated; 1,139 down-regulated), while viral infection and NIC treatment resulted in 3,617 DE genes at 16h (1,698 up-regulated; 1,919 down-regulated), although no DE genes were noted by 48h (**Figures 6E-G, Table S7**). Overrepresented GO terms with NIC treatment related to autophagosome assembly, regulation of autophagy, intracellular lipid metabolism, lipid localization and lipid homeostasis (**Figure S6**). Similar genes were noted for the effect of NIC as were with the effect of virus. RB1CC1 was up-regulated at 16h with virus infection (**Figure 6A**) but was down-regulated upon NIC treatment (**Figure 6E**) at 16h. Conversely, BMF was down-regulated with NIC at 48h, but was up-regulated upon NIC and virus treatment at 48 hours. Other genes that

were down-regulated with viral infection (GOLGA2, IFI16, WDR81, HK2, SQSTM1, ULK1) remained down-regulated with NIC treatment (with and without virus).

DISCUSSION

A virus subjugates host lipid molecules as a vehicle for entry, intracellular transport, virus replication, assembly of infectious viral particles, and egress (Miyanari et al., 2007). Ether lipids have been identified as an important lipid class for efficient membrane trafficking, endocytosis, transcytosis, and internalization of particles (Thai et al., 2001; Deng and Angelova, 2021). Deficiency of ether lipids in several model systems affects plasma membrane function, as well as structural changes in the ER and Golgi cisternae (Bazill and Dexter, 1990; Gorgas et al., 2006). SARS-CoV-2 infection has demonstrated a diverse range of COVID-19 disease severities that correlate with increased viral replication (Fajnzylber et al., 2020). Unlike during the early infection stage at 16h, where virus load and replication is low, we observed that SARS-CoV-2 infection uniquely elevated ether linked lipids after 48h of infection, a phase that represents increased virus replication, virus assembly and egress as well as host cell energy utilization (Abu-Farha et al., 2020; Dimitrov, 2004; Mazzon and Mercer, 2014). Increased viral replication drives infection severity and may lead to a perturbation of the host cellular molecular landscape (Fajnzylber et al., 2020).

We observed that NIC treatment significantly downregulates the ether lipid profile during infection. We also observed that NIC treatment in Vero E6 cells causes a reduction in TG content at both 16h and 48h suggesting a disruption of lipid droplet formation. (**Figure 4A**). NIC has previously been tested as an anti-obesity drug, and a study using it associated with a high fat diet showed a decrease in total TGs (Al-Gareeb et al., 2017). NIC also affects several lipid

species, including PE, which may stimulate the autophagy process and inhibit ether lipid elevation during viral propagation. However, NIC has dual activity in cells and is capable of influencing autophagic processes through canonical and non-canonical pathways (Liu, et al., 2019). Whereas in uninfected cells, NIC reduces autophagic flux as well as the global lipid profile (causing a decrease in plasmalogens, TGs and PE lipids), in infected cells, NIC induces autophagy and the subsequent reduction of the ether lipid profile. NIC has been shown to affect the function of lysosomes by preventing the acidification of the vacuole (Jung et al., 2019). This disruption of lysosomal function results in increased autophagic flux similar to the likely primary mechanism of action underlying the broad antiviral activity of chloroquine (Mauthe et al., 2018). Importantly, we identified that ether linked lipids were only affected by NIC treatment relative to productive virus infection at 48h, suggesting that the activity of NIC may be dependent on the cellular state or level of virus burden and virus replication kinetics.

To understand the critical lipids related to autophagy activation, we analyzed the phosphatidylethanolamine (PE) levels in NIC treated SARS-CoV-2 infected cells. PE is one of the central lipids that conjugates the factors for induction of autophagy through the formation of the autophagosome (Xie et al., 2020). We observed that the relative abundance of PE was significantly elevated with NIC treatment at 48h while there was no impact of NIC on PE levels at 16h, suggesting that NIC enhanced the autophagy machinery upon viral replication to directly affect downstream virus assembly, trafficking, and egress. Different signaling lipids such as PS, PI, and PGs play critical roles in endosome trafficking and maturation (Mazzon and Mercer, 2014) and help in infectious viral particle transport. Our study first identified that NIC treatment significantly reduced the global level of different glycerophospholipids such as PS, PI, and PG at 48h, but had no impact on early infection at 16h.

TGs are the major form of lipids enriched in lipid droplets. Drugs that stimulate TG downregulation usually activate autophagy and may prevent a cell from viral infection and pathogenesis. We identified that NIC treatment significantly reduced global levels of TGs in SARS-CoV-2 at 48h treatment, suggesting that NIC treatment potentiates TG breakdown in lipid droplets to help reduce viral replication. We also found that NIC treatment showed either no effect or very low impact on lipids that were involved in lipid droplet formation at 16h. In fasting conditions, lipid droplets are utilized for fatty acid oxidation to produce energy as intact TGs are broken down to release fatty acids in a process called lipophagy. The breakdown of TGs via hydrolysis is mediated by autophagy and we observed a decrease in TGs with NIC treatment. Overall, these findings demonstrate that NIC treatment likely activates autophagy and consequently impacts ether linked lipids and other lipids needed for viral infection and propagation.

Bis(monoacylglycerol)phosphates (BMP), identified as a new lipid of endosome-derived extracellular vehicles (EVs), also act as cholesterol transporters in cooperation with other factors and facilitate viral infection and replication (Luquain-Costaz et al., 2020). Interestingly, our study detected three different forms of BMP and two different forms of cholesterol esters (CE) that were all significantly downregulated with NIC treatment. Besides the impact of NIC on different autophagy related lipids, we also investigated the role of NIC on bioactive lipid metabolism and apoptosis. We observed a dichotomous pattern of CerNS and SM lipids, where CerNS decreased after NIC treatment (48hV vs 48hV+NIC) while SM were increased, indicative of cell death or cell survival, which may be partly explained by the cell state-dependency of NIC that we have observed in the presence or absence of SARS-CoV-2 infection in Vero E6 cells. Interestingly, we identified a notable reduction of gangliosides detected as HexCer

(which are also called glycosphingolipids) upon NIC treatment at 48h in both uninfected and SARS-CoV-2 infected Vero E6. Gangliosides have been implicated in the induction of autophagic death in mammalian cells (Hwang et al., 2010), suggesting that NIC can increase cell survival at homeostasis as well as under stress/infection conditions. This activity may in part contribute to the low cytotoxicity for this drug for several different cell lines, with the reported $CC_{50} = 50 \mu M$ (Jeon et al., 2020; Xu et al., 2020). Although gangliosides have also been shown to bind cooperatively with ACE-2 to the SARS-CoV-2 spike protein (Fantini et al., 2021), our experimental design did not include a pretreatment of cells prior to virus infection. The search for highly safe drugs for prophylaxis against COVID-19 remains elusive and controversial, but these data may suggest a role for niclosamide for future outbreaks given its broad antiviral activities. Considering the potential link between plasmalogens and the observed cytokine and lipid storms (Deng and Angelova, 2021) in severe COVID-19 patients, NIC may offer to a two-pronged treatment approach, i.e., reduce virus abundance and provide a check on an uncontrolled inflammatory response induced by SARS-CoV-2.

These findings are further supported by the global transcriptome profile that we captured for each of the treatments/conditions, wherein hallmarks of and the induction of autophagy related genes (such as DEPP1 (an autophagy regulator) (Salcher et al., 2017)), several lipases (Gassen et al., 2021), as well as genes implicated in the induction of apoptosis and genes that are markers of cell proliferation. Furthermore, GO overrepresentation analyses showed significantly upregulated terms such as death receptor activity, MAP kinase phosphatase activity, tumor necrosis factor-activated receptor activity, and phosphatidylinositol kinase activity. To investigate the role NIC has on the reversal of SARS-CoV-2 infection induced autophagy dysregulation, we explored the function of several genes that were differentially ex-

pressed. RB1CC1 (RB1 inducible Coiled-Coil 1) along with ULK1 are part of the ULK complex that initiates and regulates autophagy (Zachari and Ganley, 2017). RB1CC1 has also been shown to influence viral infection (Mauthe and Reggiori, 2016), as a depletion of RB1CC1 led to an increase of encephalomyocarditis virus replication. Here, RB1CC1 was up-regulated by SARS-CoV-2 at 16h; however, was significantly down-regulated with treatment of NIC at 16h. We also observed down-regulation of ULK1 in NIC treated cells at 16h. This elucidates the potential role of RB1CC1 and ULK1 in early infection with SARS-CoV-2 and illuminates how NIC may regulate autophagy. Interestingly, BMF was down-regulated at 48h with NIC, but up-regulated upon NIC treatment of virus infected cells at 48h. BMF encodes for a Bcl-2-modifying factor that is responsible for apoptotic regulation and has been reported as a target facilitating viral evasion (Zamaraev et al., 2020). Additionally, autophagy genes IFI16 (Duan et al., 2011; Jiang et al., 2021; Kim et al., 2020; Wichit et al., 2019), ZC3H12A (Srivastava et al., 2020), SQSTM1 (Gassen et al., 2021), WDR81 (Zhu et al., 2021), and PIK3R2 (Weisberg et al., 2020) are associated with viral infection, including SARS-CoV-1 (Gassen et al., 2021; Srivastava et al., 2020) and were downregulated in this study when cells were treated with NIC. Taken together, this provides evidence that SARS-CoV-2 infection leads to dysregulation of autophagy, and that NIC acts to reverse this effect.

Several omics studies have made a significant contribution to the identification and understanding of potential antiviral therapies for COVID-19 (Mahmud and Garrett, 2020). Bioactive molecules including PUFA lipids such as oleoylethanolamide (OEA), arachidonic acid (AA), eicosapentaenoic acid (EPA), and docosahexaenoic acid (DHA) are known from existing viral pathogenesis to inactivate enveloped viruses and inhibit pathogen proliferation/replication (Das, 2020; Ghaffari et al., 2020; Tam et al., 2013). Accumulation of lipids including

sphingolipids such as ceramides has been shown to negatively affect viral pathogenesis (Soudani et al., 2019; Young et al., 2013). Lipid metabolism; specifically catabolism, biosynthesis, and peroxidation play critical roles in autophagy or apoptosis-mediated cellular homeostasis including cell survival and death (Xie et al., 2020). Autophagy can act as an anti-viral or pro-viral mechanism; however, most viruses are found to inhibit autophagy signaling (Jackson, 2015). In the case of SARS-CoV-2, we know little about the relationship of virus infection with autophagy signaling. Importantly, we identified elevated levels of ether lipids (plasmalogen and plasmalogen) with increased viral replication, which was reported as a key lipid class for efficient membrane trafficking (Thai et al., 2001). We revealed that lipids are critical molecular factors for SARS-CoV-2 infection, entry, and viral replication into host cells. These lipids, which were elevated by SARS-CoV-2 infection may be counteracted by PUFA and VLCFA that the virus suppresses upon infection and entry (Kang et al., 2019).

Collectively, these data provide new insight into the mechanism of action for the antiviral activity of NIC, namely induction of lipophagy through the induction of autophagic pathways (**Figure 7**), which expands as well as refines our understanding of the pleiotropic antiviral mechanisms described for NIC (Braga, et al., 2021; Gassen, et al., 2021; Kao, et al., 2018). We can mechanistically infer that SARS-CoV-2 infection wrests control of cellular autophagy to ensure a productive infection of the host cell. Therapeutically, we demonstrated that NIC treatment stimulated autophagy by elevating PE levels and in parallel, downregulated total ether lipids, TGs, and other lipid molecules. Reduction of these key lipids by NIC treatment may lead to inhibition of SARS-CoV-2-induced signaling, which in turn drives viral endocytosis, vesicular trafficking, propagation, and viral egress. Activating autophagy using small molecule inhibitors/activators, oxysterols, or peptides is a promising approach for treating viral infections

(Rubinsztein et al., 2012). However, most of the potential treatments (including NIC) suffer translational obstacles due to adverse side effects, inefficient drug delivery to target tissues, and poor bioavailability (Skotland et al., 2015). Although NIC is considered an essential medicine and is well tolerated, the long history of dosing safety is based on *per os* delivery and anti-parasitic activity within the gastrointestinal tract. SARS-CoV-2 infection begins in the lungs but has been shown in several clinical studies to have a cosmopolitan infectivity profile, including the brain, heart, and gastrointestinal tract. Notably, several repurposed drugs for COVID-19 were found to be associated with autophagy induction (Kim et al., 2012), raising the possibility that some drugs that are already in clinical use for the treatment of parasitic or bacterial infections may be acting, at least in part, via autophagy. The recent clinical testing of intranasal or inhaled NIC (Backer et al., 2021) suggests that the potential of this drug for use in mitigating COVID-19 severity is profound, compelling expansive exploration of different approaches to increase targeted delivery and efficacy.

Limitations

Although we used a *C. sabaues* kidney epithelial cell line (Vero E6) and a SARS-CoV-2 strain isolated from a Floridian patient, we observed a similar (in direction and magnitude) transcriptomic response to other SARS-CoV-2 transcriptomic studies, despite differences in MOI and experimental sampling timepoints. These changes were consistent across another Vero E6 study noting cell stress and apoptosis (DeDiego et al., 2011), as well as other cell systems, including human lung cells (Wyler et al., 2021), cardiomyocytes (Sharma et al., 2020), adenocarcinomic human alveolar basal epithelial cells (Daamen et al., 2021), and bronchial epithelial cells (Yoshikawa et al., 2010), infected with different betacoronaviruses, suggesting

the responses detected herein may represent a core set of host SARS-CoV viral response genes, and that these genes are not exclusive to our study system. Our work is limited to an *in vitro* model; however, it was recently shown in a multiomics study of COVID-19 patient samples that the lipidomic profile can effectively partition COVID-19 disease severity (Overmyer et al., 2021); implying that the biology captured in our culture model is relevant *in vivo*. While these observations highlight potential utility of niclosamide, these data alone do not support its indication in the clinic in the treatment of COVID-19.

STAR METHODS

RESOURCE AVAILABILITY

Lead Contact

Further information and requests for resources and reagents should be directed to and will be fulfilled by the lead contact, Dr. Timothy Garrett (tgarrett@ufl.edu).

Materials availability

This study did not generate new unique reagents.

Data and code availability

The raw and processed data generated here have been deposited in publicly accessible databases; the RNA sequencing data is available through NCBI's GEO repository (Accession: GSE178157), and the lipidomics data is accessible via MetaboLights (Accession: MTBLS2943).

This paper does not report original code.

Any additional information required to reanalyze the data reported in this paper is available from the lead contact upon request.

EXPERIMENTAL MODEL AND SUBJECT DETAILS

Vero E6 cells.

Vero clone E6 cells (ATCC: CRL-1586) were obtained from Dr. Pei-Yong Shi (University of Texas Medical Branch). Vero E6 cells are an immortalized kidney epithelial cell line obtained from the African green monkey (*Cercopithecus sabeus*). The cells are female.

Cells were maintained at 37 °C and 5% CO₂ in Dulbecco's Modified Eagle Medium (ThermoFisher #11965118) supplemented with 10% heat-inactivated fetal bovine serum (FBS), 1X L-glutamine (Gibco #25030-081), and 1X Penicillin/Streptomycin (Corning #30-001-CI). These cells have been authenticated.

SARS-CoV-2.

SARS-CoV-2/human/USA/UF-13/2020 (GenBank: MT620766.1) was passaged in Vero E6 cells, with culture conditions as described above except using reduced serum media with 3% FBS rather than 10% FBS. Virus was collected after 4 days to establish a low passage virus stock within our biosafety level 3 (BSL-3) laboratory at the Emerging Pathogens Institute.

METHOD DETAILS

Cell culture, infection, and niclosamide treatment.

Cells were seeded in 6 well plates at a density of 500,000 cells/well. Each replicate sample represents an individual plate well, with three biological replicates per condition, per time point. The investigators were not blinded to the conditions. At hour zero (48 hours post seeding), media was removed and replaced with reduced serum Dulbecco's Modified Eagle Medium

(supplemented with 3% FBS, 1X L-glutamine, and 1X Penicillin/Streptomycin) to facilitate infection.

One vial of SARS-CoV-2 stock was thawed and diluted to a titer of 2×10^7 plaque forming units (PFU) per mL. For infected conditions, virus was inoculated into each well with 12.5 μ L of diluted virus stock for a multiplicity of infection (MOI) of 0.5 infectious virus particles/ Vero E6 cell. Niclosamide (MedChemExpress #HY-B0497, [NIC]) stock was dissolved in molecular grade DMSO and added to the indicated wells for a final concentration of 5 μ M (0.5% v/v DMSO final concentration). An equivalent amount of molecular grade DMSO was used as a vehicle control. This concentration of NIC was selected to have antiviral effect but be well below the observed 50% cytotoxic concentration (CC_{50}) of the drug (50 μ M) to avoid inadvertent cell lysis in treated conditions (Wu et al., 2004).

Samples were prepared and collected following a time of addition experimental design (Daelemans et al., 2011) as follows (**Figure 1, Table S1A-B**). The “0 hour” (0h) samples were collected 48h after cell seeding. The “16 hour” (16h) conditions were infected with virus, treated with NIC or DMSO at hour zero, and harvested at hour 16 of the experiment (**Figure 1**). The “48 hour” (48h) conditions were infected with virus at hour zero, supernatant was removed after 24h, and cells were treated with NIC or DMSO in fresh media. Cells were harvested at hour 48. Uninfected samples (with and without drug treatment) were also prepared and collected as above. For samples from infected conditions, the supernatant was removed at the indicated harvest timepoint, taking care not to disturb the cell monolayer, and retained at -80°C. The cells were washed once with 1X PBS. The PBS wash was removed and 0.25% trypsin-EDTA (ThermoFisher #25200056) was added to each well. The plates were then incubated at 37°C and 5% CO₂ for 5-10 minutes until cells had completely detached from the cell

surface. Trypsinization was halted by the addition of 1 mL FBS. The supernatant was removed, the cell pellet was resuspended in 1X PBS, and the sample was centrifuged at 700 RPM for 5 minutes. Supernatant was aspirated, and 100% methanol was added to each sample purposed for lipid analysis. Alternatively, 750 μ L of TRIzol reagent (ThermoFisher #15596026) was added to each sample purposed for RNASeq. All samples were stored at -80°C until analysis. For uninfected conditions, harvest proceeded the same as described above except trypsinization was halted using 4 mL of complete Dulbecco's Modified Eagle Medium instead of FBS, and pellets were flash frozen in liquid nitrogen instead of being resuspended in a chemical inactivation agent after the last centrifugation step. All samples were stored at -80°C until analysis.

Global lipid extraction.

Cell pellets from each time point and condition were extracted using a modified Folch biphasic extraction procedure (Ulmer, et al. 2017). Samples were pre-normalized to the protein concentration (800 μ g/mL) obtained using a Qubit 4.0 Fluorometer (Thermo Fisher Scientific). Lipids were extracted using ice cold 4:2:1 chloroform:methanol:water (v:v:v) containing 20 μ L of a 10X diluted internal standard mixture (stock solution of 50 ppm, w: v), and the organic phase was collected after centrifugation at 3260 $\times g$ for 5 min at 4°C, dried under nitrogen gas, and reconstituted in 75 μ L of Isopropanol (IPA) plus 1 μ L of injection standard mixture (100 ppm, w:v). Internal standards used in this analysis covered a range of lipid classes and structures including: lysophosphatidylcholine (LPC 17:0), phosphatidylcholine (PC 17:0/17:0), phosphatidylethanolamine (PE 15:0/15:0), phosphatidylserine (PS 14:0/14:0), phosphatidylglycerol (PG 14:0/14:0), ceramide (Cer d18:1/17:0), diacylglycerol (DG 14:0/14:0), and sphingomyelin (SM d18:1/7:0). For injection standards, triacylglycerol (TG 17:0/17:0/17:0),

487 LPC 19:0, PE 17:0/17:0, PS 17:0/17:0, and PG 17:0/17:0 were used. Except for TG, all other
 488 lipid standards were purchased from Avanti Polar Lipids (Alabaster, AL) while TG was pur-
 489 chased from Sigma Aldrich. All lipid standards were diluted prior to analysis in 1:2 (v/v) chloro-
 490 form:methanol (CHCl_3 :MeOH) and a working standard mix was then prepared by diluting the
 491 stock solution with the same solvent mixture.

492 **LC-MS-based lipid data collection and analysis.**

493 Ultra-high-pressure liquid chromatography coupled to high resolution mass spectrometry
 494 (UHPLC-HRMS) was used for data collection. Chromatographic separation was achieved us-
 495 ing reversed phase chromatography (Dionex Ultimate 3000 RS UHPLC system, Thermo Sci-
 496 entific) with a Waters Acquity C18 BEH column (2.1 × 50 mm, 1.7 μm) (Waters, Milford, MA,
 497 US). The mobile phases consisted of solvent A (60:40 acetonitrile:water) and solvent B
 498 (90:8:2) isopropanol:acetonitrile:water), both containing 10 mM ammonium formate and 0.1%
 499 formic acid. The flow rate was 500 $\mu\text{L}/\text{min}$ and the column temperature was maintained at
 500 50°C. A multi-step gradient was used for separation starting with 0% B from 0-1 min, increas-
 501 ing to 30% B from 1-3 min, then up to 45% B from 3-4 min, 60% B from 4-6 min, 65% B from
 502 6-8 min, held at 65% B from 8-10 min, increased to 90% B from 10-15 min, then increased to
 503 98% B from 15-17 min and finally held at 98% B from 17-18 min before returning to initial con-
 504 ditions to equilibrate for the next injection. Samples were analyzed in positive and negative
 505 electrospray ionization as separate injections on a ThermoScientific Q-Exactive high resolution
 506 mass spectrometer (Thermo Scientific, San Jose, CA). Lipidomics data were compiled and an-
 507 notated using LipidMatch (Koelmel et al., 2017).

508 **RNA extraction.**

509 For total RNA extraction from flash frozen cells, the cell pellet was thawed on ice. Cell pellets
 510 were resuspended in 1 mL Trizol, and 200 μ L chloroform was added to each sample. Samples
 511 were mixed thoroughly by vortexing, then incubated at room temperature for 3 minutes. Sam-
 512 ples were centrifuged at 12,000 xg for 15 minutes at 4°C. The upper aqueous layer was trans-
 513 ferred to a new tube and 500 μ L isopropanol was added and mixed by vortexing, prior to incu-
 514 bation at room temperature for 10 minutes. RNA was pelleted by centrifuging at 12,000 xg for
 515 10 minutes at 4°C, and supernatant was discarded. The pellet was rinsed in 75% ethanol and
 516 pelleted by centrifuging at 7,500 xg for 5 minutes at 4°C. The ethanol wash and spin were re-
 517 peated a second time. The pellet was air dried in an inverted tube. Genomic DNA was digest-
 518 ed using the TURBO DNA-free™ Kit (Invitrogen #AM1907) according to manufacturer instruc-
 519 tions. Samples were mixed with 350 μ L buffer RLT from the RNeasy® Mini kit (Qiagen
 520 #74104) and 250 μ L 100% ethanol, then transferred to a RNeasy® Mini kit spin column. Col-
 521 umns were centrifuged at 8,000 xg for 15 seconds at room temperature, and flow-through was
 522 discarded. Buffer RPE (500 μ L) was added to the column, which was centrifuged at the same
 523 conditions, and flow-through was discarded. The RPE wash was repeated a second time. The
 524 column was transferred to a fresh collection tube and centrifuged at 12,000 xg for 1 min to dry.
 525 RNA was eluted by adding 50 μ L of nuclease free water and centrifuging for 1 minute at 8,000
 526 xg and was immediately frozen at -80°C. To extract viral RNA from culture supernatant, super-
 527 natant was thawed, 200 μ L of supernatant was mixed with 200 μ L DNA/RNA Shield, and RNA
 528 was immediately extracted using the Quick-DNA/RNA™ Viral MagBead kit (Zymo Research
 529 #R2140), according to manufacturer instructions and then immediately frozen at -80°C.

Real-time RT-qPCR.

To quantify viral genome copy in supernatant, one step real time reverse transcription qPCR (RT-qPCR) was performed using 4x Quantabio UltraPlex 1-Step ToughMix No Rox (VWR #10804-946) and CDC 2019-nCoV_N1 (nucleocapsid) primer and probe mix (see Key Resources Table for primer and probe sequences) at a final concentration of 22.5 μ M, in a 20 μ L reaction volume with 5 μ L template. All samples were run in technical duplicates. RT-qPCR was run on a BioRad CFX96™ Real-Time System. The thermal cycling conditions were as follows: 50°C for 20 minutes, 94°C for 2 min; followed by 45 cycles of 94°C for 15 seconds, 55°C for 30 seconds, and 68°C for 10 seconds. The samples were quantified using a standard curve generated using a 2019-nCoV_N_Positive Control plasmid (IDT # 10006625). Standard curve points were plotted in Microsoft Excel v.2102 and cycle threshold values of unknown samples were determined from the logarithmic line of best fit equation to calculate genome copies/mL.

RNASeq analysis.

All 27 RNA samples (see **Table S1A-B**) were directly sent to Novogene (<https://en.novogene.com/>), where in-house RNA quality control and library preparation was performed. Libraries were sequenced on an Illumina NovaSeq6000 platform using a 150bp kit with paired-end read mode.

Mapping, expression, and pathway analyses.

Bioinformatic processing was completed using Galaxy (<https://galaxyproject.org>, (Batut et al., 2018)). Quality control was performed with Cutadapt v 1.16 (Martin, 2011) and FastQC v 0.11.8 (<http://www.bioinformatics.babraham.ac.uk/projects/fastqc/>) to remove adapters, <20 nucleotide reads and low-quality reads. RNA STAR v2.7.7a (Dobin et al., 2013) was used to map samples to the *Chlorocebus sabaeus* genome and associated annotation (GenBank ac-

cession # GCA_015252025.1). featureCounts v 2.0.1 (Liao et al., 2014) was used with Infer Experiment v2.6.4.1 (Wang et al., 2012) to determine the strandedness of the samples, and sum reads for each gene. Read counts for each sample were input into DESeq2 v 1.22.1 (Love et al., 2014) to call differential gene expression, analyzing the effect of time, drug, and virus on the samples. Resultant differential expression files were manually annotated using a combination of NCBI (O’Leary et al., 2016) and Ensembl (Yates et al., 2020) due to the poor annotation quality of the genome (https://www.ncbi.nlm.nih.gov/genome/annotation_euk/Chlorocebus_sabaeus/100/). Significantly regulated gene names were separately parsed out for each comparison and uploaded to ENRICHR (Kuleshov et al., 2016) for downstream gene ontology (GO (Harris et al., 2004)) and pathway analyses using Reactome (Fabregat et al., 2016), MSigDB (Liberzon et al., 2015), and KEGG (Ogata et al., 1999)) databases.

QUANTIFICATION AND STATISTICAL ANALYSIS

Unless indicated in the figure legend, all experiments were performed in triplicate and results are presented as mean \pm standard error of mean (SEM) of absolute values or percentages of control. Each replicate was a separate tissue culture well processed in parallel. A list of all samples used for subsequent analysis can be seen in **Table S1A-B**.

Statistical P-values were obtained by application of the appropriate statistical tests using GraphPad Prism v.9.0. Lipidomics data was normalized to the total ion signal, log transformed, autoscaled and analyzed with Metaboanalyst v.3.0 (Pang et al., 2021). For quality control, internal lipid standards added to each sample were used to assess technical reproducibility, achieving $\leq 15\%$ relative standard deviation (RSD) across all samples. Correlation

heatmaps were generated for the lipid samples using Pearson's r . Heatmap clustering was performed using a T-test or an ANOVA, showing the most significant lipids. For lipidomics applications, Bonferroni false discovery rate (FDR) adjusted P-values lower than 0.05 and an absolute fold-change greater than or equal to 1.5 were considered significant. For RNASeq differential gene expression, gene ontology and pathway analyses, statistical significance was corrected for multiple comparisons (Bonferroni adjusted) and assessed at an $\alpha=0.05$. Genes with absolute \log_2 fold changes ≥ 1 were considered significantly differentially expressed. For supernatant genome copy RT-qPCR, a two-way non-parametric ANOVA with Dunn's post-hoc test was performed in GraphPad Prism v.6.0 and assessed at an $\alpha=0.05$. Since no statistical differences were observed between technical replicates of the same condition in the supernatant genome copy RT-qPCR data, technical replicate wells were pooled in the reported analysis.

AUTHOR INFORMATION

Corresponding Author

Contact information for the author(s) to whom correspondence should be addressed:

Rhoel R. Dinglasan rdinglasan@epi.ufl.edu and Timothy J. Garrett tgarrett@ufl.edu

Acknowledgements

This work was funded in part by support from the University of Florida Preeminence Initiative through the College of Veterinary Medicine and the Emerging Pathogens Institute (RRD).

Author Contributions

597 The manuscript was written through contributions by all authors. RRD, TG and JAL conceptu-
598 alized the study. IM, HC, TH, CJS, and JA conducted the study and generated samples and
599 data. IM, HC, TH, MM, JA, HSY, RRD and TG analyzed the data. IM, HC, TH, MM, JA, JAL,
600 RRD and TG wrote/edited the manuscript. All authors have given approval to the final version
601 of the manuscript.

602 ‡These authors contributed equally.

603 Declaration of Interests

604 The authors declare no competing interests.

605 REFERENCES

606 Abu-Farha, M., Thanaraj, T.A., Qaddoumi, M.G., Hashem, A., Abubaker, J., and Al-Mulla, F.
607 (2020). The Role of Lipid Metabolism in COVID-19 Virus Infection and as a Drug Target. *Int. J.*
608 *Mol. Sci.* 21.

609 Al-Gareeb Al, Aljubory KD, Alkuraishy HM. Niclosamide as an anti-obesity drug: an experi-
610 mental study. *Eat Weight Disord.* 2017 Jun;22(2):339-344. doi: 10.1007/s40519-017-0373-1.
611 Epub 2017 Mar 7. PMID: 28271456.

612 Axfors, C., Schmitt, A.M., Janiaud, P., Van't Hooft, J., Abd-El salam, S., Abdo, E.F., Abella,
613 B.S., Akram, J., Amaravadi, R.K., Angus, D.C., et al. (2021). Mortality outcomes with
614 hydroxychloroquine and chloroquine in COVID-19 from an international collaborative meta-
615 analysis of randomized trials. *Nat. Commun.* 12, 2349.

616 Backer V, Sjöbring U, Sonne J, Weiss A, Hostrup M, Johansen HK, Becker V, Sonne DP,
617 Balchen T, Jellingsø M, Sommer MOA. (2021) A randomized, double-blind, placebo-controlled
618 phase 1 trial of inhaled and intranasal niclosamide: A broad spectrum antiviral candidate for
619 treatment of COVID-19. *Lancet Reg Health Eur.* 4, 100084.

620 Batut, B., Hiltemann, S., Bagnacani, A., Baker, D., Bhardwaj, V., Blank, C., Bretaudeau, A.,
621 Brillet-Guéguen, L., Čech, M., Chilton, J., et al. (2018). Community-Driven Data Analysis Train-
622 ing for Biology. *Cell Syst.* 6, 752–758.e1.

623 Bazill, G.W., and Dexter, T.M. (1990). Role of endocytosis in the action of ether lipids on
624 WEHI-3B, HL60, and FDCP-mix A4 cells. *Cancer Res.* 50, 7505–7512.

625 Borba, M.G.S., Val, F.F.A., Sampaio, V.S., Alexandre, M.A.A., Melo, G.C., Brito, M., Mourão,
626 M.P.G., Brito-Sousa, J.D., Baía-da-Silva, D., Guerra, M.V.F., et al. (2020). Effect of High vs
627 Low Doses of Chloroquine Diphosphate as Adjunctive Therapy for Patients Hospitalized With
628 Severe Acute Respiratory Syndrome Coronavirus 2 (SARS-CoV-2) Infection: A Randomized
629 Clinical Trial. *JAMA Netw. Open* 3, e208857.

630 Braga, L., Ali, H., Secco, I., Chiavacci, E., Neves, G., Goldhill, D., Penn, R., Jimenez-
631 Guardado, J.M., Ortega-Prieto, A.M., Bussani, R., et al. (2021) Drugs that inhibit TMEM16 pro-
632 teins block SARS-CoV-2 spike-induced syncytia. *Nature* 594, 88-93.

633 Di Cara, F., Maile, T.M., Parsons, B.D., Magico, A., Basu, S., Tapon, N., and King-Jones, K.
634 (2015). The Hippo pathway promotes cell survival in response to chemical stress. *Cell Death*
635 *Differ.* 22, 1526–1539.

636 D'Alessandro, S., Scaccabarozzi, D., Signorini, L., Perego, F., Ilboudo, D.P., Ferrante, P., and
637 Delbue, S. (2020). The Use of Antimalarial Drugs against Viral Infection. *Microorganisms* 8.

638 Daamen, A.R., Bachali, P., Owen, K.A., Kingsmore, K.M., Hubbard, E.L., Labonte, A.C., Robl,
639 R., Shrotri, S., Grammer, A.C., and Lipsky, P.E. (2021). Comprehensive transcriptomic analy-
640 sis of COVID-19 blood, lung, and airway. *Sci Rep.* 11, 7052.

641 Daelemans, D., Pauwels, R., De Clercq, E., and Pannecouque, C. (2011). A time-of-drug addi-
642 tion approach to target identification of antiviral compounds. *Nat. Protoc.* 6, 925–933.

643 Das, U.N. (2020). Can Bioactive Lipids Inactivate Coronavirus (COVID-19)? *Arch Med Res* 51,
644 282–286.

645 DeDiego, M.L., Nieto-Torres, J. L., Jiménez-Guardado, Regla-Nava, J.A., Alvarez, E.,
646 Oliveros, J.C., Zhao, J., Fett, C., Perlman, S., and Enjuanes, L. (2011). Severe acute respirato-

647 ry syndrome coronavirus envelope protein regulates cell stress response and apoptosis. PLoS
648 Pathog. 7, e1002315.

649 Deng, Y., and Angelova, A. (2021). Coronavirus-Induced Host Cubic Membranes and Lipid-
650 Related Antiviral Therapies: A Focus on Bioactive Plasmalogens. Front. Cell Dev. Biol. 9,
651 630242.

652 Dimitrov, D.S. (2004). Virus entry: molecular mechanisms and biomedical applications. Nat.
653 Rev. Microbiol. 2, 109–122.

654 Dobin, A., Davis, C.A., Schlesinger, F., Drenkow, J., Zaleski, C., Jha, S., Batut, P., Chaisson,
655 M., and Gingeras, T.R. (2013). STAR: ultrafast universal RNASeq aligner. Bioinformatics 29,
656 15–21.

657 Dong, E., Du, H., and Gardner, L. (2020). An interactive web-based dashboard to track
658 COVID-19 in real time. Lancet Infect. Dis. 20, 533–534.

659 Duan, X., Ponomareva, L., Veeranki, S., & Choubey, D. (2011). IFI16 induction by glucose re-
660 striction in human fibroblasts contributes to autophagy through activation of the
661 ATM/AMPK/p53 pathway. *PloS one*, 6(5), e19532.
662 <https://doi.org/10.1371/journal.pone.0019532>

663 Dyal, J., Coleman, C.M., Hart, B.J., Venkataraman, T., Holbrook, M.R., Kindrachuk, J., John-
664 son, R.F., Olinger, G.G., Jahrling, P.B., Laidlaw, M., et al. (2014). Repurposing of clinically de-
665 veloped drugs for treatment of Middle East respiratory syndrome coronavirus infection.
666 Antimicrob. Agents Chemother. 58, 4885–4893.

667 Ewers, H., and Helenius, A. (2011). Lipid-mediated endocytosis. Cold Spring Harb. Perspect.
668 Biol. 3, a004721.

669 Fabregat, A., Sidiropoulos, K., Garapati, P., Gillespie, M., Hausmann, K., Haw, R., Jassal, B.,
670 Jupe, S., K€orninger, F., McKay, S., et al. (2016). The Reactome pathway Knowledgebase. Nu-
671 cleic Acids Res. 44, D481–7.

- 672 Fantini, J., Chahinian, H., Yahi, N. (2020). Leveraging coronavirus binding to gangliosides for
673 innovative vaccine and therapeutic strategies against COVID-19. *Biochem Biophys Res*
674 *Commun.* 29, 132-136.
- 675 Fajnzylber, J., Regan, J., Coxen, K., Corry, H., Wong, C., Rosenthal, A., Worrall, D., Giguel,
676 F., Piechocka-Trocha, A., Atyeo, C., et al. (2020). SARS-CoV-2 viral load is associated with
677 increased disease severity and mortality. *Nat. Commun.* 11, 5493.
- 678 Gassen, N.C., Niemeyer, D., Muth, D., Corman, V.M., Martinelli, S., Gassen, A., Hafner, K.,
679 Papies, J., Mösbauer, K., Zellner, A., et al. (2019). SKP2 attenuates autophagy through
680 Beclin1-ubiquitination and its inhibition reduces MERS-Coronavirus infection. *Nat. Commun.*
681 10, 5770.
- 682 Gassen, N.C., Papies, J., Bajaj, T. et al. (2021) SARS-CoV-2-mediated dysregulation of me-
683 tabolism and autophagy uncovers host-targeting antivirals. *Nat Commun* 12, 3818
- 684 Gautret, P., Lagier, J.-C., Parola, P., Hoang, V.T., Meddeb, L., Mailhe, M., Doudier, B.,
685 Courjon, J., Giordanengo, V., Vieira, V.E., et al. (2020). Hydroxychloroquine and azithromycin
686 as a treatment of COVID-19: results of an open-label non-randomized clinical trial. *Int. J.*
687 *Antimicrob. Agents* 56, 105949.
- 688 Ghaffari, S., Roshanravan, N., Tutunchi, H., Ostadrahimi, A., Pouraghaei, M., and Kafil, B.
689 (2020). Oleoylethanolamide, A Bioactive Lipid Amide, as A Promising Treatment Strategy for
690 Coronavirus/COVID-19. *Arch Med Res* 51, 464–467.
- 691 Goldman, D.L., Aldrich, M.L., Hagmann, S.H.F., Bamford, A., Camacho-Gonzalez, A.,
692 Lapadula, G., Lee, P., Bonfanti, P., Carter, C.C., Zhao, Y., et al. (2021). Compassionate Use of
693 Remdesivir in Children With Severe COVID-19. *Pediatrics* 147, e2020047803.
- 694 Gordon, D.E., Jang, G.M., Bouhaddou, M., Xu, J., Obernier, K., White, K.M., O'Meara, M.J.,
695 Rezelj, V.V., Guo, J.Z., Swaney, D.L., et al. (2020). A SARS-CoV-2 protein interaction map re-
696 veals targets for drug repurposing. *Nature* 583, 459–468.
- 697 Gorgas, K., Teigler, A., Komljenovic, D., and Just, W.W. (2006). The ether lipid-deficient
698 mouse: tracking down plasmalogen functions. *Biochim. Biophys. Acta* 1763, 1511–1526.

699 Harris, M.A., Clark, J., Ireland, A., Lomax, J., Ashburner, M., Foulger, R., Eilbeck, K., Lewis,
700 S., Marshall, B., Mungall, C., et al. (2004). The Gene Ontology (GO) database and informatics
701 resource. *Nucleic Acids Res.* 32, D258–61.

702 Hwang J., Lee H.J., Lee W.H., Suk K. (2010). NF- κ B as a common signaling pathway in
703 ganglioside-induced autophagic cell death and activation of astrocytes *J Neuroimmunol.*
704 226(1-2), 66-72.

705 Jackson, W.T. (2015). Viruses and the autophagy pathway. *Virology* 479-480, 450–456.

706 Jeon, S., Ko, M., Lee, J., Choi, I., Byun, S.Y., Park, S., Shum, D., and Kim, S. (2020). Identifi-
707 cation of Antiviral Drug Candidates against SARS-CoV-2 from FDA-Approved Drugs.
708 *Antimicrob. Agents Chemother.* 64 ,e00819-20.

709 Ji, W., Wang, W., Zhao, X., Zai, J., and Li, X. (2020). Cross-species transmission of the newly
710 identified coronavirus 2019-nCoV. *J. Med. Virol.* 92, 433–440.

711 Jiang Z, Wei F, Zhang Y, Wang T, Gao W, Yu S, Sun H, Pu J, Sun Y, Wang M, Tong Q, Gao
712 C, Chang KC, Liu J. (2021). IFI16 directly senses viral RNA and enhances RIG-I transcription
713 and activation to restrict influenza virus infection. *Nat Microbiol* 6, 932–945.

714 Kang, K.W., Kim, S., Cho, Y.-B., Ryu, S.R., Seo, Y.-J., and Lee, S.-M. (2019). Endogenous n-3
715 Polyunsaturated Fatty Acids Are Beneficial to Dampen CD8+ T Cell-Mediated Inflammatory
716 Response upon the Viral Infection in Mice. *Int. J. Mol. Sci.* 20, 4510.

717 Kao, J.C., HuangFu, W.C., Tsai, T.T., Ho, M.R., Jhan, M.K., Shen, T.J., Tseng, P.C., Wang,
718 Y.T., Lin, C.F. (2018). The antiparasitic drug niclosamide inhibits dengue virus infection by in-
719 terfering with endosomal acidification independent of mTOR. *PLoS Negl Trop Dis.* 12,
720 e0006715. doi:

721 Kim B, Arcos S, Rothamel K, Jian J, Rose KL, McDonald WH, Bian Y, Reasoner S, Barrows
722 NJ, Bradrick S, Garcia-Blanco MA, Ascano M. (2020). Discovery of Widespread Host Protein
723 Interactions with the Pre-replicated Genome of CHIKV Using VIR-CLASP. *Mol Cell* 78, 624-
724 640.e7.

Kim, J.-J., Lee, H.-M., Shin, D.-M., Kim, W., Yuk, J.-M., Jin, H.S., Lee, S.-H., Cha, G.-H., Kim, J.-M., Lee, Z.-W., et al. (2012). Host cell autophagy activated by antibiotics is required for their effective antimycobacterial drug action. *Cell Host Microbe* 11, 457–468.

Koelmel, J.P., Kroeger, N.M., Ulmer, C.Z., Bowden, J.A., Patterson, R.E., Cochran, J.A., Beecher, C.W.W., Garrett, T.J., and Yost, R.A. (2017). LipidMatch: an automated workflow for rule-based lipid identification using untargeted high-resolution tandem mass spectrometry data. *BMC Bioinformatics* 18, 331.

Koyuncu, E., Purdy, J.G., Rabinowitz, J.D., and Shenk, T. (2013). Saturated very long chain fatty acids are required for the production of infectious human cytomegalovirus progeny. *PLoS Pathog.* 9, e1003333.

Kuleshov, M.V., Jones, M.R., Rouillard, A.D., Fernandez, N.F., Duan, Q., Wang, Z., Koplev, S., Jenkins, S.L., Jagodnik, K.M., Lachmann, A., et al. (2016). Enrichr: a comprehensive gene set enrichment analysis web server 2016 update. *Nucleic Acids Res.* 44, W90–7.

Liao, Y., Smyth, G.K., and Shi, W. (2014). featureCounts: an efficient general purpose program for assigning sequence reads to genomic features. *Bioinformatics* 30, 923–930.

Liberzon, A., Birger, C., Thorvaldsdóttir, H., Ghandi, M., Mesirov, J.P., and Tamayo, P. (2015). The Molecular Signatures Database (MSigDB) hallmark gene set collection. *Cell Syst.* 1, 417–425.

Liu Y, Luo X, Shan H, Fu Y, Gu Q, Zheng X, Dai Q, Xia F, Zheng Z, Liu P, Yin XM, Hong L, Li M. (2019). Niclosamide Triggers Non-Canonical LC3 Lipidation. *Cells* 2019 8, 248.

Liu, J., Cao, R., Xu, M., Wang, X., Zhang, H., Hu, H., Li, Y., Hu, Z., Zhong, W., and Wang, M. (2020). Hydroxychloroquine, a less toxic derivative of chloroquine, is effective in inhibiting SARS-CoV-2 infection in vitro. *Cell Discov.* 6, 16.

Love, M.I., Huber, W., and Anders, S. (2014). Moderated estimation of fold change and dispersion for RNASeq data with DESeq2. *Genome Biol.* 15, 550.

750 Luquain-Costaz, C., Rabia, M., Hullin-Matsuda, F., and Delton, I. (2020).
751 Bis(monoacylglycero)phosphate, an important actor in the host endocytic machinery hijacked
752 by SARS-CoV-2 and related viruses. *Biochimie* 179, 247–256.

753 Mahmud, I., and Garrett, T.J. (2020). Mass Spectrometry Techniques in Emerging Pathogens
754 Studies: COVID-19 Perspectives. *J Am Soc Mass Spectrom* 31, 2013–2024.

755 Marsh, M., and Helenius, A. (2006). Virus entry: open sesame. *Cell* 124, 729–740.

756 Martin, M. (2011). Cutadapt removes adapter sequences from high-throughput sequencing
757 reads. *EMBnet j.* 17, 10.

758 Mauthe, M., & Reggiori, F. (2016). ATG proteins: Are we always looking at autophagy?
759 *Autophagy*, 12(12), 2502–2503. <https://doi.org/10.1080/15548627.2016.1236878>

760 Mauthe, M., Orhon, I., Rocchi, C., Zhou, X., Luhr, M., Hijlkema, K.-J., Coppes, R.P., Engedal,
761 N., Mari, M., and Reggiori, F. (2018). Chloroquine inhibits autophagic flux by decreasing
762 autophagosome-lysosome fusion. *Autophagy* 14, 1435–1455.

763 Mazzon, M., and Mercer, J. (2014). Lipid interactions during virus entry and infection. *Cell*
764 *Microbiol.* 16, 1493–1502.

765 Miyanari, Y., Atsuzawa, K., Usuda, N., Watashi, K., Hishiki, T., Zayas, M., Bartenschlager, R.,
766 Wakita, T., Hijikata, M., and Shimotohno, K. (2007). The lipid droplet is an important organelle
767 for hepatitis C virus production. *Nat. Cell Biol.* 9, 1089–1097.

768 Nguyen, A., Guedán, A., Mousnier, A., Swieboda, D., Zhang, Q., Horkai, D., Le Novere, N.,
769 Solari, R., and Wakelam, M.J.O. (2018). Host lipidome analysis during rhinovirus replication in
770 HBECs identifies potential therapeutic targets. *J. Lipid Res.* 59, 1671–1684.

771 O’Leary, N.A., Wright, M.W., Brister, J.R., Ciufo, S., Haddad, D., McVeigh, R., Rajput, B.,
772 Robbertse, B., Smith-White, B., Ako-Adjei, D., et al. (2016). Reference sequence (RefSeq) da-
773 tabase at NCBI: current status, taxonomic expansion, and functional annotation. *Nucleic Acids*
774 *Res.* 44, D733–45.

775 Ogata, H., Goto, S., Sato, K., Fujibuchi, W., Bono, H., and Kanehisa, M. (1999). KEGG: kyoto
776 encyclopedia of genes and genomes. *Nucleic Acids Res.* 27, 29–34.

777 Overmyer, K.A., Shishkova, E., Miller, I.J., Balnis, J., Bernstein, M.N., Peters-Clarke, T.M.,
778 Meyer, J.G., Quan, Q., Muehlbauer, L.K., Trujillo, E.A., et al. (2021). Large-Scale Multi-omic
779 Analysis of COVID-19 Severity. *Cell Syst.* 12, 23–40.e7.

780 Pacha, O., Sallman, M.A., and Evans, S.E. (2020). COVID-19: a case for inhibiting IL-17? *Nat.*
781 *Rev. Immunol.* 20, 345–346.

782 Pang, Z., Chong, J., Zhou, G., Morais D., Chang, L., Barrette, M., Gauthier, C., Jacques, P.E.,
783 Li, S., and Xia, J. (2021) [MetaboAnalyst 5.0: narrowing the gap between raw spectra and func-](#)
784 [tional insights](#) *Nucl. Acids Res.* (doi: 10.1093/nar/gkab382)

785 Pindiprolu, S.K.S.S., and Pindiprolu, S.H. (2020). Plausible mechanisms of Niclosamide as an
786 antiviral agent against COVID-19. *Med. Hypotheses* 140, 109765.

787 Rizvi, Z.A., Dalal, R., Sadhu, S., Kumar, Y., Shrivastava, T., Gupta, S.K., Agarwal, S., Tripathy,
788 M.R., Yadav, A.K., Medigeshi, G.R., et al. (2021). Immunological and cardio-vascular patholo-
789 gies associated with SARS-CoV-2 infection in golden syrian hamster. *BioRxiv*.

790 Rubinsztein, D.C., Codogno, P., and Levine, B. (2012). Autophagy modulation as a potential
791 therapeutic target for diverse diseases. *Nat. Rev. Drug Discov.* 11, 709–730.

792 Salcher, S., Hermann, M., Kiechl-Kohlendorfer, U., Ausserlechner, M.J., Obexer, P. (2017)
793 C10ORF10/DEPP-mediated ROS accu-mulation is a critical modulator of FOXO3-induced au-
794 tophagy. *Mol Cancer.* 16, 95.

795 Sharma, A., Garcia Jr., G., Wang, Y., Plummer, J. T., Morizono, K., Arumugaswami, V., and
796 Svendsen, C. N. (2020). Human iPSC-Derived Cardiomyocytes Are Susceptible to SARS-
797 CoV-2 Infection. *Cell Rep Med.* 1, 100052.

798 Skotland, T., Iversen, T.G., Torgersen, M.L., and Sandvig, K. (2015). Cell-penetrating pep-
799 tides: possibilities and challenges for drug delivery in vitro and in vivo. *Molecules* 20, 13313–
800 13323.

801 Soudani, N., Hage-Sleiman, R., Karam, W., Dbaiho, G., and Zaraket, H. (2019). Ceramide
802 suppresses influenza A virus replication in vitro. *J. Virol.* 93.

803 Srivastava, R., Daulatabad, S. V., Srivastava, M., & Janga, S. C. (2020). Role of SARS-CoV-2
804 in Altering the RNA-Binding Protein and miRNA-Directed Post-Transcriptional Regulatory Net-
805 works in Humans. *International journal of molecular sciences*, 21(19), 7090.
806 <https://doi.org/10.3390/ijms21197090>

807 Stukalov, A., Girault, V., Grass, V., Karayel, O., Bergant, V., Urban, C., Haas, D.A., Huang, Y.,
808 Oubraham, L., Wang, A., et al. (2021). Multilevel proteomics reveals host perturbations by
809 SARS-CoV-2 and SARS-CoV. *Nature*.

810 Tam, V.C., Quehenberger, O., Oshansky, C.M., Suen, R., Armando, A.M., Treuting, P.M.,
811 Thomas, P.G., Dennis, E.A., and Aderem, A. (2013). Lipidomic profiling of influenza infection
812 identifies mediators that induce and resolve inflammation. *Cell* 154, 213–227.

813 Thai, T.P., Rodemer, C., Jauch, A., Hunziker, A., Moser, A., Gorgas, K., and Just, W.W.
814 (2001). Impaired membrane traffic in defective ether lipid biosynthesis. *Hum. Mol. Genet.* 10,
815 127–136.

816 Ulmer C.Z., Yost R.A., and Garrett T.J. (2017) Global UHPLC/HRMS Lipidomics Workflow for
817 the Analysis of Lymphocyte Suspension Cultures. In: Wood P. (eds) *Lipidomics*.
818 *Neuromethods*, vol 125. Humana Press, New York, NY. [https://doi.org/10.1007/978-1-4939-](https://doi.org/10.1007/978-1-4939-6946-3_13)
819 [6946-3_13](https://doi.org/10.1007/978-1-4939-6946-3_13)

820 V'kovski, P., Kratzel, A., Steiner, S., Stalder, H., and Thiel, V. (2020). Coronavirus biology and
821 replication: implications for SARS-CoV-2. *Nat. Rev. Microbiol.* 19, 155–170.

822 Vincent, M.J., Bergeron, E., Benjannet, S., Erickson, B.R., Rollin, P.E., Ksiazek, T.G., Seidah,
823 N.G., and Nichol, S.T. (2005). Chloroquine is a potent inhibitor of SARS coronavirus infection
824 and spread. *Virol. J.* 2, 69.

825 Weisberg, E., Parent, A., Yang, P. L., Sattler, M., Liu, Q., Liu, Q., Wang, J., Meng, C.,
826 Buhrlage, S. J., Gray, N., & Griffin, J. D. (2020). Repurposing of Kinase Inhibitors for Treat-

827 ment of COVID-19. *Pharmaceutical research*, 37(9), 167. [https://doi.org/10.1007/s11095-020-](https://doi.org/10.1007/s11095-020-02851-7)
828 02851-7

829 Wang, L., Wang, S., and Li, W. (2012). RSeQC: quality control of RNASeq experiments. *Bioin-*
830 *formatics* 28, 2184–2185.

831 Wang, M., Cao, R., Zhang, L., Yang, X., Liu, J., Xu, M., Shi, Z., Hu, Z., Zhong, W., and Xiao,
832 G. (2020). Remdesivir and chloroquine effectively inhibit the recently emerged novel corona-
833 virus (2019-nCoV) in vitro. *Cell Res.* 30, 269–271.

834 Wichit, S., Hamel, R., Yainoy, S., Gumpangseth, N., Panich, S., Phuadraksa, T., Saetear, P.,
835 Monteil, A., Morales Vargas, R., & Missé, D. (2019). Interferon-inducible protein (IFI) 16 regu-
836 lates Chikungunya and Zika virus infection in human skin fibroblasts. *EXCLI journal*, 18, 467–
837 476. <https://doi.org/10.17179/excli2019-1271>

838 Wu, C.-J., Jan, J.-T., Chen, C.-M., Hsieh, H.-P., Hwang, D.-R., Liu, H.-W., Liu, C.-Y., Huang,
839 H.-W., Chen, S.-C., Hong, C.-F., et al. (2004). Inhibition of severe acute respiratory syndrome
840 coronavirus replication by niclosamide. *Antimicrob. Agents Chemother.* 48, 2693–2696.

841 Wyler, E., Mösbauer, K., Franke, V., Diag, A., Gottula, L.T., Arsiè, R., Klironomos, F.,
842 Koppstein, D., Hönzke, K., Ayoub, S., Buccitelli, C., Hoffmann, K., Richter, A., Legnini, I.,
843 Ivanov, A., Mari, T., Del Giudice, S., Papies, J., Praktiknjo, S., Meyer, T.F., Müller, M.A., Nie-
844 meyer, D., Hocke, A., Selbach, M., Akalin, A., Rajewsky, N., Drosten, C., and Landthaler, M.
845 (2021). Transcriptomic profiling of SARS-CoV-2 infected human cell lines identifies HSP90 as
846 target for COVID-19 therapy. *iScience.* 24, 102151.

847 Xie, Y., Li, J., Kang, R., and Tang, D. (2020). Interplay between lipid metabolism and autophagy.
848 *Front. Cell Dev. Biol.* 8, 431.

849 Xu, J., Shi, P.-Y., Li, H., and Zhou, J. (2020). Broad spectrum antiviral agent niclosamide and
850 its therapeutic potential. *ACS Infect. Dis.* 6, 909–915.

851 Yates, A.D., Achuthan, P., Akanni, W., Allen, J., Allen, J., Alvarez-Jarreta, J., Amode, M.R.,
852 Armean, I.M., Azov, A.G., Bennett, R., et al. (2020). Ensembl 2020. *Nucleic Acids Res.* 48,
853 D682–D688.

- 854 Young, M.M., Kester, M., and Wang, H.-G. (2013). Sphingolipids: regulators of crosstalk be-
855 tween apoptosis and autophagy. *J. Lipid Res.* *54*, 5–19.
- 856 Yoshikawa, T., Hill, T.E., Yoshikawa, N., Popov, V.L., Galindo, C.L., Garner, H.R., Peters, C.J.,
857 and Kent Tseng, C. (2010). Dynamic innate immune responses of human bronchial epithelial
858 cells to severe acute respiratory syndrome-associated coronavirus infection. *PLoS One.* *5*,
859 e8729.
- 860 Zachari, M., & Ganley, I. G. (2017). The mammalian ULK1 complex and autophagy initia-
861 tion. *Essays in biochemistry*, *61*(6), 585–596. <https://doi.org/10.1042/EBC20170021>
- 862 Zamaraev AV, Zhivotovsky B, Kopeina GS. Viral Infections: Negative Regulators of Apoptosis
863 and Oncogenic Factors. *Biochemistry (Mosc).* 2020 Oct;*85*(10):1191-1201. doi:
864 10.1134/S0006297920100077. PMID: 33202204; PMCID: PMC7590567.
- 865 Zhou, Y., Hou, Y., Shen, J., Huang, Y., Martin, W., and Cheng, F. (2020). Network-based drug
866 repurposing for novel coronavirus 2019-nCoV/SARS-CoV-2. *Cell Discov.* *6*, 14.
- 867 Zhu, Y., Feng, .F, Hu, G., Wan,g Y., Yu, Y., Zhu, Y., Xu, W., Cai, X., Sun, Z., Han, W., Ye, R.,
868 Qu, D., Ding, Q., Huang, X., Chen, H., Xu, W., Xie, Y., Cai, Q., Yuan, Z., Zhang, R. (2021). A
869 genome-wide CRISPR screen identifies host factors that regulate SARS-CoV-2 entry. *Nat*
870 *Commun.* *12*, 961.

871

872 **FIGURE LEGENDS**

873 **Figure 1. Workflow for lipidomic and transcriptomic profiling of Vero E6 cells after**
874 **SARS-CoV-2 infection with and without niclosamide treatment.** We used a time-of-
875 addition assay experimental design to (i) capture the lipidomic profile of SARS-CoV-2 infected
876 Vero E6 cells, and (ii) explore the effect of niclosamide on the lipidomic profile of Vero E6 cells
877 when added in the absence of infection, with SARS-CoV-2 virus, or at 24h post-infection. Each
878 replicate experimental condition (n=3) was processed for LC-HRMS/MS or RNASeq analyses.
879 Samples were seeded 48h prior to the start of the experiment (t = 0h). For all samples, media

was changed at the start of the experiment (t = 0h) and infected with virus (for infected sample groups). Sample collection is denoted by an up arrow and tube above the timeline, media changes are denoted by red bottles, addition of virus and DMSO/drug are denoted as well. Separate samples for each condition were collected for LC-HRMS/MS and RNAseq analysis, respectively.

Figure 2. Global lipidomics analysis in SARS-CoV-2 infected Vero E6 cells at 16h and 48h. (A) Hierarchical cluster heatmap analysis depicting the major affected lipid clustering between 16h and 48h infection. (B) Volcano plot showing the differential lipid abundance with SARS-CoV-2 infection between 16h and 48h. The primary significant upregulated lipids were ether-linked (plasmayl and plasmeyl). (C) Bar graph showing the total abundance of ether lipids between the time points. (D) Extracted ion chromatogram comparison showing relative peak intensity of a single ether lipid between 16h (blue) and 48h (magenta) infection. The arrow points to the lipid identified as Plasmayl-PC (O-18:0/16:0)+H at retention time 9.16. Identification was confirmed by accurate mass and MS/MS.

Figure 3. Comparison of individual lipid classes at early (16h) and late (48h) viral infection. FDR P-value based on T-test shown above each plot. Individual triangles represent each lipid detected and expression compared at both time points. Abbreviations: TG-triglycerides, DG-diglycerides, CL-cardiolipin, CE-cholesterol ester, SM-sphingomyelin, PC-phosphatidylcholine, PE-phosphatidylethanolamine, PS-phosphatidylserine, PI-phosphatidylinositol, PG-phosphatidylglycerol, LPC-lysophosphatidylcholine, LPE-

902 lysophosphatidylethanolamine, oxLPC-oxidized lysophosphatidylcholine, HexCer-
903 hexosylceramide, CerNS-ceramide with non-hydroxy fatty acid, n.s.-not significant.

904

905 **Figure 4. Niclosamide modulates lipid metabolism in Vero E6 cells in the absence of**
906 **SARS-CoV-2 infection.** Heatmap showing the changes in neutral lipids across the time points
907 with and without NIC (A). Bar graphs of the significant lipids at 16h vs 48h (B) and 48h vs 48h
908 + NIC (C). Fold change of less than 1.5 and p-value less than or equal to 0.05.

909

910 **Figure 5. Niclosamide (NIC) impact ether-linked lipid production during viral replication**
911 **at 48h.** (A) Heatmap of the top 70 lipids (Fold change ≥ 1.5 and p-value ≤ 0.05). (B) Volcano
912 plot showing the significant up and down regulated lipids with NIC at 48h. (C) The total ether
913 lipids were down regulated with NIC treatment.

914

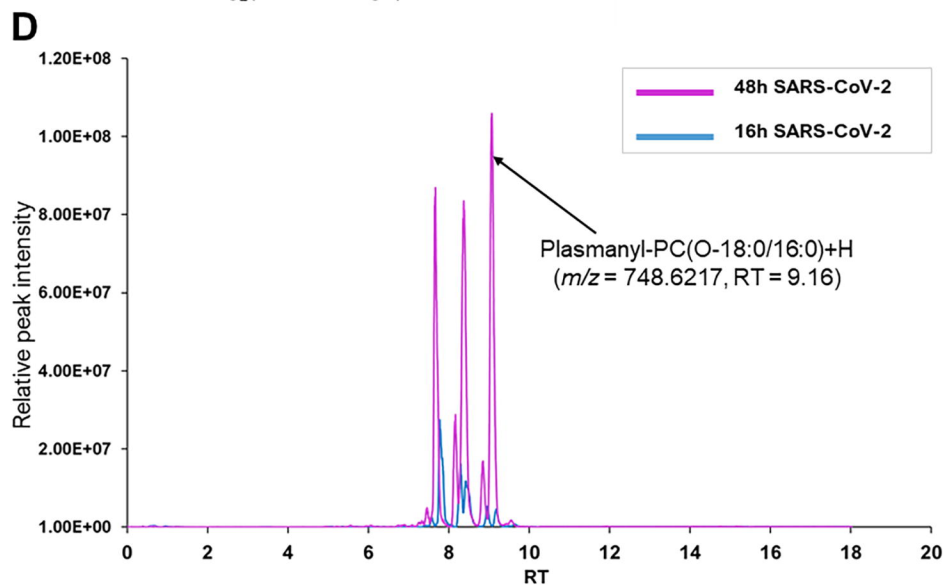
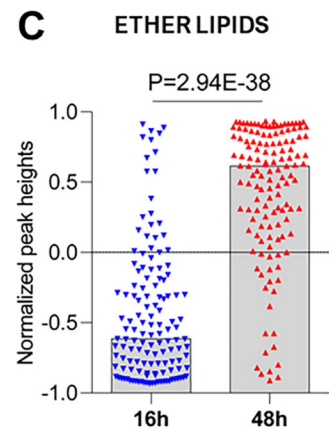
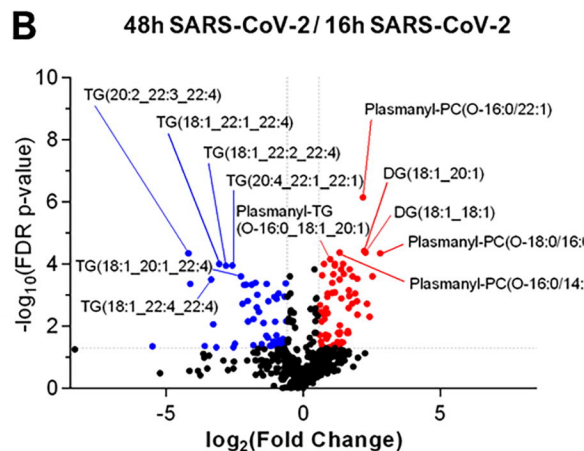
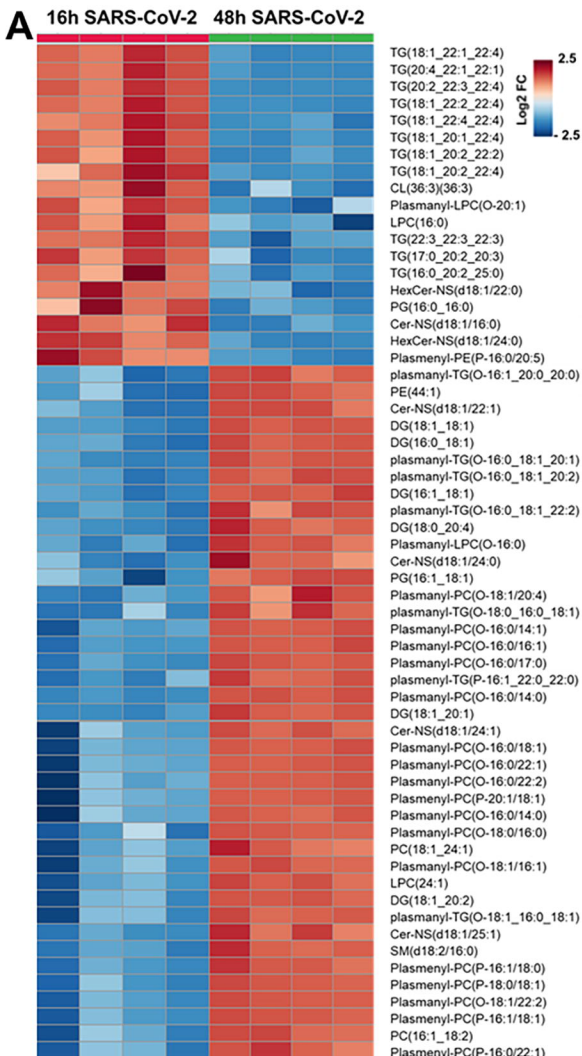
915 **Figure 6. Significantly expressed genes across SARS-CoV-2 and Niclosamide condi-**
916 **tions.** Genes were designated as significantly expressed using DESeq2 when their Bonferroni
917 adjusted P-value was ≤ 0.05 , and the $|\log_2(\text{Fold Change})|$ was ≥ 1 . Each dot represents an indi-
918 vidual gene. Blue dots are significantly downregulated genes, red dots are significantly
919 upregulated genes, and grey dots are not significantly differentially expressed genes. (A)
920 DMSO treated no virus versus DMSO treated, virus samples at 16 hours, (B) DMSO treated no
921 virus versus DMSO treated virus samples at 48 hours, (C) Niclosamide treated no virus versus
922 niclosamide treated virus samples at 16 hours, (D) Niclosamide treated no virus versus
923 niclosamide treated virus samples at 48 hours, (E) DMSO treated no virus versus niclosamide

924 treated no virus samples at 16 hours, (F) DMSO treated no virus versus niclosamide treated
 925 no virus samples at 48 hours, (G) DMSO treated virus versus niclosamide treated virus sam-
 926 ples at 16 hours, (H) DMSO treated virus at 16 hours versus 48 hours, (I) Niclosamide treated,
 927 no virus samples at 16 vs 48 hours.

928

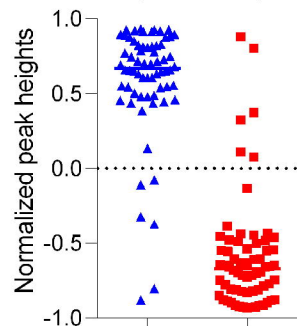
929 **Figure 7. The effect of SARS-CoV-2 infection and NIC treatment on host cell lipid me-**
 930 **tabolism.** SARS-CoV-2 infection in Vero E6 cells alters host cell lipid metabolism during early
 931 and late stages of infection. Increased transcription of lipid receptors LRP2 and VLDLR, and
 932 phosphorylation signaling regulators are observed throughout viral infection. Changes in TG
 933 composition from unsaturated to saturated acyl-chains occurs as a function of viral replication,
 934 with an overall decrease in TG lipids at late infection timepoints. This change corresponds with
 935 an increase to DG and BMP lipids that is indicative of energy consumption and incorporation
 936 into membranes and vesicles, activation of autophagy pathways, as well as impacting viral rep-
 937 lication. Treatment of cells with NIC alters lipid composition and gene regulation corresponding
 938 to apoptosis and autophagy related pathways. Decreases to ether lipids (TGs and DGs) and
 939 BMP are observed and reflect a decrease to exocytosis pathways for viral egress.

940

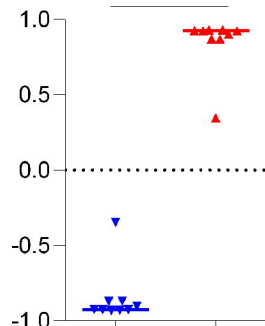


TG

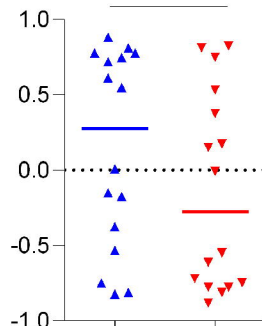
P=3.51E-37

**DG**

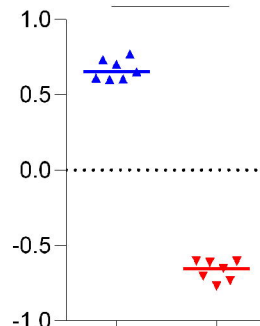
P=2.14E-12

**CL**

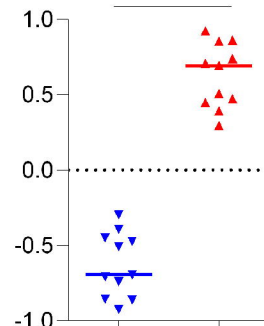
n.s.

**CE**

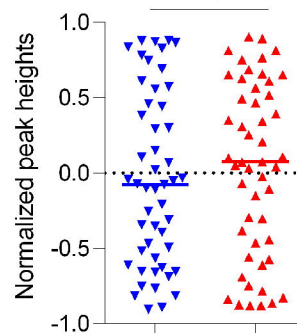
P=1.09E-13

**SM**

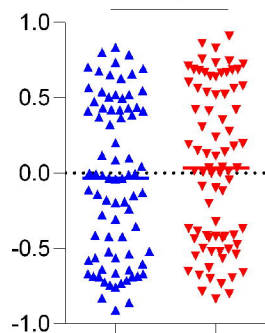
P=1.10E-11

**PC**

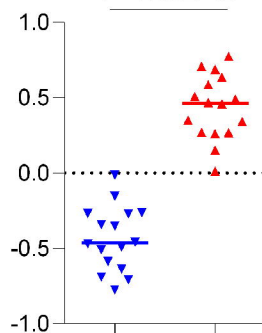
n.s.

**PE**

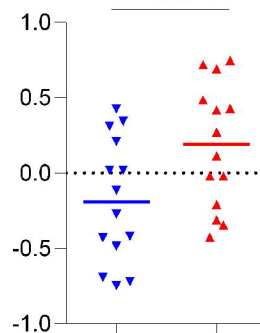
n.s.

**PS**

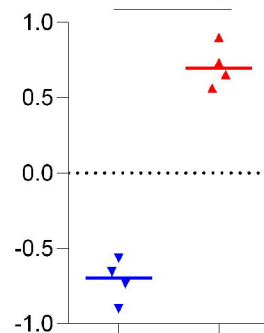
P=1.48E-12

**PI**

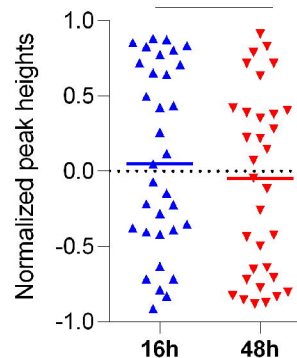
P=0.027

**PG**

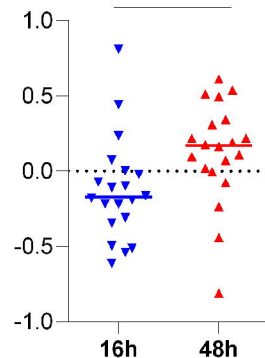
P=7.52E-06

**LPC**

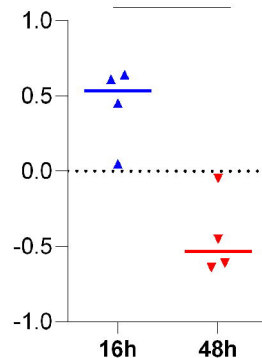
n.s.

**LPE**

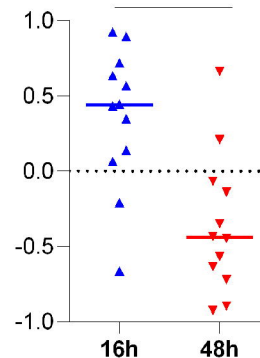
P=0.024

**oxLPC**

P=0.0039

**HexCer**

P=0.001

**CerNS**

P=0.034

